Lab on a Chip

RSC Publishing

PAPER

View Article Online
View Journal | View Issue

Single cell detection using a magnetic zigzag nanowire biosensor

Cite this: *Lab Chip*, 2013, **13**, 3098

Hao-Ting Huang, Tzong-Rong Ger, Ya-Hui Lin and Zung-Hang Wei*

A magnetic zigzag nanowire device was designed for single cell biosensing. Nanowires with widths of 150, 300, 500, and 800 nm were fabricated on silicon trenches by electron beam lithography, electron beam evaporation, and lift-off processes. Magnetoresistance measurements were performed before and after the attachment of a single magnetic cell to the nanowires to characterize the magnetic signal change due to the influence of the magnetic cell. Magnetoresistance responses were measured in different magnetic field directions, and the results showed that this nanowire device can be used for multi-directional detection. It was observed that the highest switching field variation occurred in a 150 nm wide nanowire when the field was perpendicular to the substrate plane. On the other hand, the highest magnetoresistance ratio variation occurred in a 800 nm wide nanowire also when the field was perpendicular to the substrate plane. Besides, the trench-structured substrate proposed in this study can fix the magnetic cell to the sensor in a fluid environment, and the stray field generated by the corners of the magnetic zigzag nanowires has the function of actively attracting the magnetic cells for detection.

Received 12th April 2013,
Accepted 16th May 2013

DOI: 10.1039/c3lc50457c

www.rsc.org/loc

Introduction

A wide variety of methods have been used for sensing individual micro-scale magnetic labels. Coils or SQUID are conventional methods. Recently, sensors based on anisotropic magnetoresistance, giant magnetoresistance, spin valves, and so on, have drawn a great deal of attention due to their high sensitivity.[1] So far, most of those magnetoresistance sensors are all similar to the sensors in hard disk drives for recording applications, and are yet to be designed for bio applications. Magnetoresistance-based biosensors possess several advantages including high sensitivity and receiving less interference from the environment, and are therefore suitable for sensitive bio-detectors.[2–4] Besides, the magnetic stray field emitted from biological specimens is not shielded by chemical compounds, microstructures or other biomaterials, so the signals detected by the magnetoresistance-based biosensors are not influenced by the surrounding objects. Optical biosensors, however, may suffer from disadvantages such as limited optical signals available for trace detection. Besides, the optical signals of the analytes may be influenced by the surrounding chemical compounds, microstructures and other biomaterials, so incorrect analysis might occur. Another drawback of optical biosensors is that the inorganic compounds, such as cadmium, frequently used in quantum dot light sources, and heavy metal ions are highly toxic to biological systems.[5]

Department of Power Mechanical Engineering, National Tsing Hua University, Hsinchu 300, Taiwan. E-mail: wei@pme.nthu.edu.tw

So far, magnetoresistive biosensors have mainly been used to detect magnetic nanoparticles attached to specific biomolecules. This technique is suitable for trace detection.[6–11] Magnetic particles are of great interest to biomedical technology researchers due to their low toxicity,[12] good biocompatibility and stability as well as their superparamagnetic properties, and they are widely used in the applications of magnetic transportation and positioning,[13,14] purification and separation,[15–17] magnetic resonance imaging,[18–20] drug delivery,[21–23] thermal therapy,[24,25] and so on. The sensing mechanism of magnetoresistive biosensors is based on the specific binding between antibodies that are fixed on the sensor surface and antigens that are labeled with magnetic nanoparticles. After washing away the biomolecules that are not specifically binding to the sensor surface, the magnetoresistance biosensors detect the magnetic nanoparticles carried by the antigens [see Fig. 1(a)].

There have been some studies on the detection of magnetic particles[26–29] and biomolecules[30–32] using magnetoresistance sensors. When the antigens labeled with magnetic nanoparticles bind to the antibodies on the biosensor surface, the distance between the magnetic nanoparticles and the sensor surface is only a few nanometers to tens of nanometers [see Fig. 1(a)]. As for a cell that contains magnetic nanoparticles inside, the magnetic nanoparticles might be separated from the sensor surface by the organelles and the cytoplasm, so the distance between the magnetic nanoparticles and the sensor surface exhibits a wide distribution on the scale of micrometers [see Fig. 1(b)]. Fig. 1(c) shows the scanning electron microscope (SEM) image of a magnetic NPC-TW01 cell on the

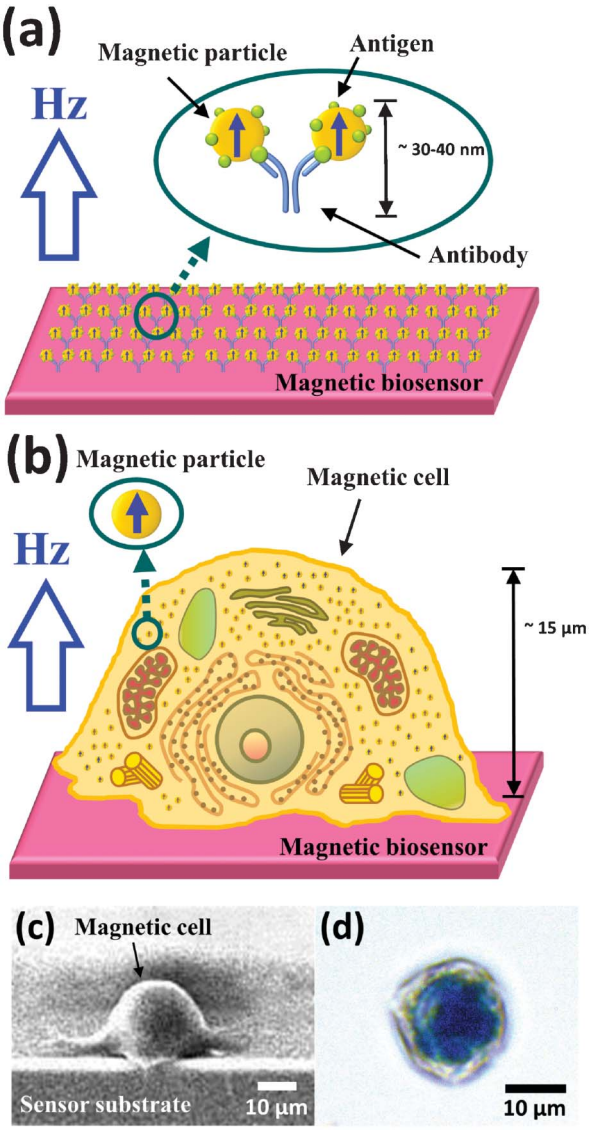

Fig. 1 Schematics for the size scale of the magnetoresistance-based biosensors with respect to the analytes of (a) biomolecules and (b) a cell. (c) SEM imaging of a magnetic cell on the sensor surface. (d) Magnetic cell after Prussian blue staining (Fe^{3+}-specific) which was used for observing the distribution of magnetic nanoparticles.

sensor substrate after the cell was treated by fixation, dehydration and drying procedures. It was observed that the height of the cell was about 15 μm. Fig. 1(d) shows the magnetic cell after Prussian blue staining (Fe^{3+}-specific) which was used for observing the distribution of magnetic nanoparticles. Besides, the magnetic nanoparticles might be suspended or flowing in the cell, not like the case where the magnetic nanoparticles are fixed *via* the interaction between antigens and antibodies. Therefore, detecting bio cells labeled with magnetic nanoparticles using magnetoresistance biosensors is more challenging compared to detecting specifically binding biomolecules such as antigens and antibodies, and the technique still needs to be verified. Moreover, single cell detection is very important in cancer cell detection[33] and cell dynamics studies.[34,35] However, for most cases, only the response of a group of cells rather than a single cell can be obtained using current biosensing techniques. Therefore, it is imperative to develop magnetoresistance biosensors for single cell detection.

Experimental methods

I. Magnetic cell preparation and characterization

In our experiment, nasopharyngeal cancer cells (NPC-TW01), which are a type of adherent cells, were cultured in Dulbecco's modified Eagle's medium (DMEM) that consisted of 1% penicillin and 10% fetal calf serum at 37 °C and under a 5% CO_2 environment. The cells were then co-cultured in diluted magnetic fluid (Ferrotec EMG 705) with a concentration of 2 μg ml^{-1}. The magnetic fluid was comprised of Fe_3O_4 magnetic nanoparticles, each with a diameter of 10 nm. After 24 h of co-culturing, a significant number of magnetic nanoparticles entered the cells through endocytosis. Subsequently, the cells that contained magnetic nanoparticles were collected by a magnet, concentrated by centrifugation, and then put in a clean culture solution.[36]

Magnetophoresis[37,38] was performed in our study to estimate the number of magnetic nanoparticles in a cell. An external magnetic field gradient was applied to the cells, which led to a distribution of cell velocities as shown in Fig. 2. When the viscous force $F_{vis} = 6\pi\eta v R_{cell}$, given by Stokes' law, and the magnetic force $F_{mag} = m_{particles} dB/dx$ exerted on a cell under a magnetic field gradient dB/dx were balanced, the cell moved at a constant velocity v as shown in the inset of Fig. 2. The parameters η, v, R_{cell}, and $m_{particles}$ represent the viscosity of the medium, cell velocity, radius of the cell, and total magnetic moment of the magnetic nanoparticles inside a cell, respectively. The velocity distribution of the cells shown in Fig. 2 was derived from observation using an optical microscope, and it was calculated cell by cell for a total of 300 cells. The balance between the viscous force and the magnetic force can be expressed as:

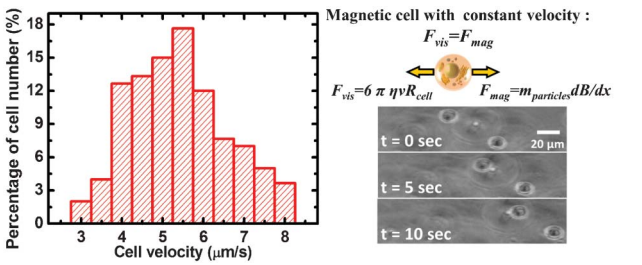

Fig. 2 Cell velocity distribution obtained by magnetophoresis. NPC-TW01 cells were co-cultured with 2 μg ml^{-1} EMG-705 solution for 24 h for magnetic labeling. When the viscous force (F_{vis}) and magnetic force (F_{mag}) balanced out, the magnetic cell moved at a constant velocity as shown in the sequential OM images. The number of the magnetic cells counted was 300. The average velocity obtained for these cells was (5.532 ± 1.195) μm s^{-1}. The average quantity of the magnetic nanoparticles absorbed by a cell was estimated to be (5.835 ± 1.260) × 10^6.

$$6\pi\eta v R_{\text{cell}} = m_{\text{particles}} \frac{\mathrm{d}B}{\mathrm{d}x} \quad (1)$$

The total magnetic moment of the magnetic nanoparticles inside a cell was given by $m_{\text{particles}} = NcM_s\pi D^3/6$ where N is the total number of magnetic nanoparticles per cell, D is the diameter of a magnetic nanoparticle, and c is the ratio of the net magnetization of magnetic nanoparticles to their saturation magnetization M_s. According to the experimental results obtained in a previous report,[39] the parameter c can be set as 0.8. Therefore, using eqn (1), the number N of magnetic nanoparticles per cell can be estimated to be 5.835×10^6.

II. Device design and fabrication

A smart magnetic biosensor should not only possess high sensitivity but should also be able to attract and fix the magnetic cell onto the sensor for detection. In this design, the magnetic particles on the apexes and valleys of the zigzag magnetic nanowires can actively attract the magnetically labeled cells onto the nanowires for detection. Besides, the fluid flow in a microfluidic chip is relatively fast for cells, and it might wash away the cells even when the magnetic cells are attached to the magnetic thin film of the magnetoresistive biosensor, especially for a low-frictional flat surface. Therefore, the designed magnetic nanowire biosensors on zigzag trenches can also reinforce the attachment of the cells to the sensors.[40]

Comparing with photolithography, e-beam lithography is more flexible for making patterns ranging from the nanoscale to the microscale. The nanowires that were adopted in our device can be easily prepared using e-beam lithography rather than photolithography. Besides, mask-free e-beam lithography is in general more flexible and versatile for various experimental tests in laboratories. The fabrication process of the zigzag nanowires is shown in Fig. 3. Six windows 4 μm wide with a 2 μm interval were defined on a silicon substrate with a 20 nm oxide layer using e-beam lithography. The six oxide windows that were not covered by PMMA were completely removed by a buffered oxide etchant (BOE) [see Fig. 3(a)]. The six windows whose oxide layer was removed were anisotropically etched by tetramethylammonium hydroxide (TMAH) and formed a trench structure with a depth of 2.8 μm [see Fig. 3(b)]. Subsequently, BOE etching was performed to remove the remaining oxide around the trenches [see Fig. 3(c)]. In the next step, the patterns of nanowires with widths of 150, 300, 500, and 800 nm were defined on the Si trench using e-beam

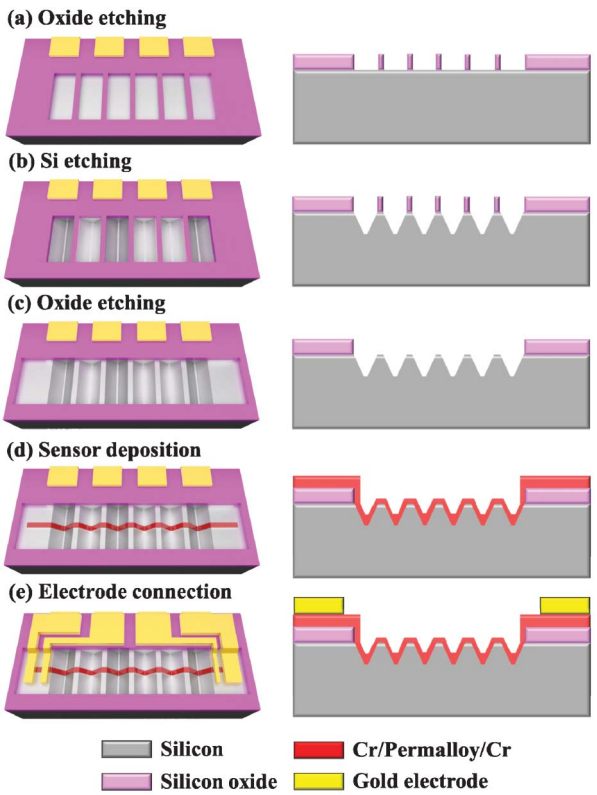

Fig. 3 The fabrication process of a permalloy nanowire on a zigzag surface. The left column represents the top view, and the right column represents the lateral view.

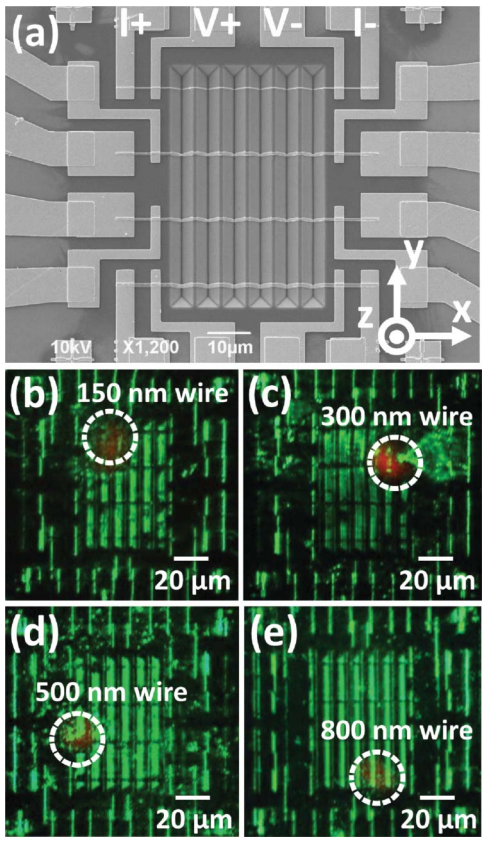

Fig. 4 (a) SEM image of the permalloy nanowires on the zigzag trenches. The widths of the nanowires from top to bottom are 150, 300, 500, and 800 nm, respectively. Four-probe measurements were performed to measure the magnetoresistance curves with a magnetic field applied along the x, y, and z axes. (b)–(e) Fluorescence images of single magnetic cells attached to the permalloy nanowire with 150, 300, 500, and 800 nm width, respectively. The magnetic cells, indicated by the white dashed circles, were dyed in red whereas the surrounding green glow is the reflection of the exciting laser.

lithography, and thin films of Cr(10 nm)/permalloy(100 nm)/Cr(10 nm) were then deposited using an e-beam evaporator. The bottom Cr layer served as an adhesive layer and the top Cr layer served as a protective layer that could prevent the permalloy layer from corroding in solution. During the deposition process, a quartz crystal was used to detect the film thickness; the substrate was kept at room temperature and no magnetic field was applied. The pressure was kept at 10^{-7} torr and the deposition rate was 0.5 Å s^{-1}. After the lift-off process in acetone, the entire photoresistor was removed and the magnetic zigzag nanowire thin films were obtained on the trench substrate [see Fig. 3(d)]. In the final step, gold electrodes were deposited for four-probe measurement through similar procedures using e-beam lithography, e-beam evaporation, and lift-off processes [see Fig. 3(e)]. Fig. 4(a) shows the SEM image of the zigzag permalloy nanowires with widths of 150, 300, 500, and 800 nm. The fluorescent images of the zigzag nanowires attached to a magnetic cell (stained in red) are shown in Fig. 4(b)–4(e).

Results and discussions

We applied a magnetic field along the x, y, and z axes (see Fig. 4(a)), and measured the magnetoresistance curves of the nanowires before and after the attachment of magnetic cells by a four-probe method. The switching field of the magnetic nanowire can be defined as the field in which the magnetoresistance has an abrupt change in the magnetization process as indicated in Fig. 5(a). H_{c_0} is the average of the switching field in the sweep-down and sweep-up processes when there is no magnetic cell attached on the sensor device; when there is a magnetic cell attached on the sensor device, the averaged switching field is H_{c_1}. When the magnetic field is applied along the hard axis of the nanowire, the full width at half maximum (FWHM) of the curve is used to characterize the response of the sensor as indicated in Fig. 5(b). The magnetoresistance ratio is defined as $\Delta R/R_s$, where R_s is the magnetoresistance at the saturation field and ΔR is the difference between the highest and the lowest magnetoresistance. The original switching field, full width at half maximum, and magnetoresistance ratio of the bare device were H_{c_0}, FWHM_0, and $\mathrm{MRratio}_0$, respectively. When a magnetic cell was attached to the sensor device, the corresponding variations were ΔH_c, ΔFWHM and MRratio, respectively. The sensitivities of the sensor device were determined by the normalized values: $\Delta H_c/H_{c_0}$, $\Delta\mathrm{FWHM}/\mathrm{FWHM}_0$, and $\Delta\mathrm{MRratio}/\mathrm{MRratio}_0$. The larger the normalized values, the higher the sensitivity.

Fig. 6 represents the magnetoresistance curves when no magnetic cells were attached to the nanowires. Fig. 6(a) and 6(b) show the magnetoresistance curves of the permalloy

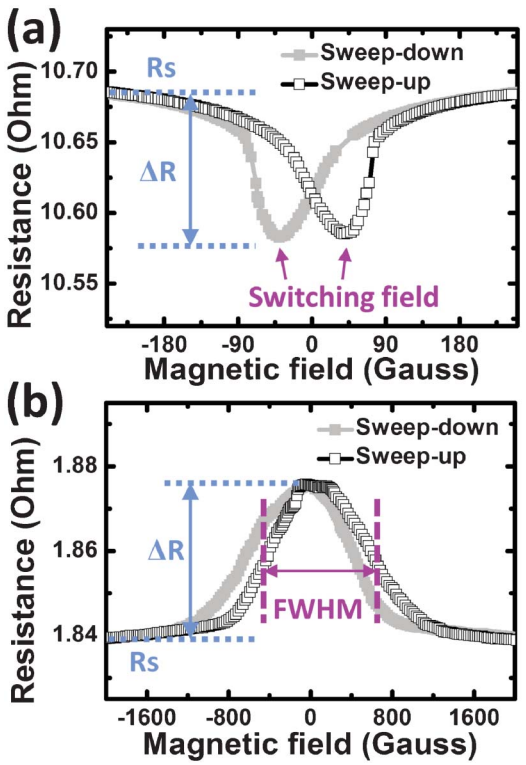

Fig. 5 The definitions of (a) switching field and (b) FWHM from the magnetoresistance curves of a typical magnetic nanowire when the magnetic field is applied along the magnetic easy axis and hard axis, respectively.

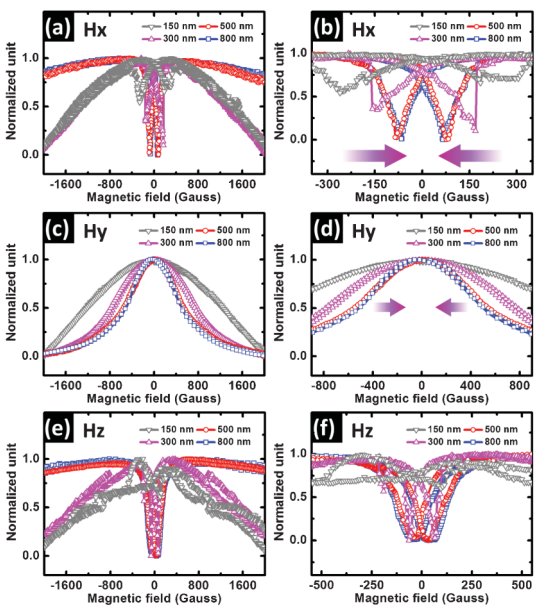

Fig. 6 (a) and (b) Magnetoresistance curves of the nanowires with widths of 150, 300, 500, and 800 nm. The magnetic field was swept along the x axis and the switching fields were found to be 255.50, 155.50, 79.07, and 66.13 Gauss for the four nanowires, respectively; the magnetoresistance ratios were 0.0412%, 0.0593%, 0.2356%, and 0.2801%, respectively. (c) and (d) Magnetoresistance curves of the same set of nanowires when the field was swept along the y axis. The FWHM was 2465.98, 1512.53, 1073.65, and 987.76 Gauss for the four nanowires, respectively; the magnetoresistance ratios were 0.6710%, 0.6527%, 0.5927%, and 0.5126%, respectively. (e) and (f) Magnetoresistance curves of the same set of nanowires when the field was swept along the z axis. The switching fields were 100.50, 63.50, 35.72, and 29.78 Gauss for the four nanowires, respectively; the magnetoresistance ratios were 0.0235%, 0.0559%, 0.2372%, and 0.2685%, respectively.

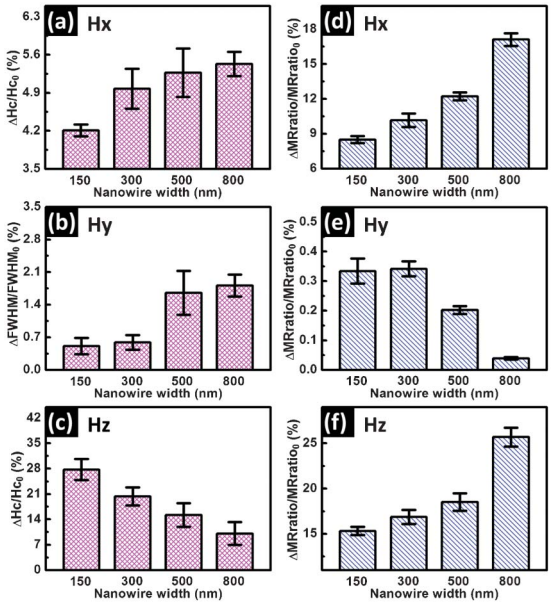

Fig. 7 Reduced variations of the (a) and (d) switching field and magnetoresistance ratio, (b) and (e) FWHM and magnetoresistance ratio, and (c) and (f) switching field and magnetoresistance ratio when the field was along the *x*, *y*, and *z* axes, respectively. H_{c_0}, $FWHM_0$ and $MRratio_0$ were the initial values where no magnetic cells were attached, and ΔH_c, ΔFWHM and ΔMRratio were the variations when magnetic cells were attached.

nanowires when an external magnetic field was applied along the *x* axis. We observed that the narrower the nanowire, the larger the switching field and the lower the magnetoresistance ratio. Fig. 6(c) and 6(d) show the magnetoresistance curves of the permalloy nanowires when the field was along the *y* axis, which is the magnetic hard axis of the nanowires. In this case, the narrower wire width kept the magnetization from tilting away from the magnetic easy axis, thereby increasing the full width at half maximum (FWHM) of the curve. Fig. 6(e) and 6(f) represent the magnetoresistance curves when the field was along the *z* axis, and it can be observed that the variations of the switching fields and the magnetoresistance ratios for the nanowires with different widths were not as profound as the case in which the field was along the *x* axis.

Fig. 7 represents the reduced variations of the switching field, magnetoresistance ratio, and FWHM of the zigzag nanowires after the attachment of a single magnetic cell. The results in Fig. 7(a) and 7(c) show that the switching fields profoundly changed after the attachment of magnetic cells when the field was applied along the *x* and *z* axes, respectively. When a *z*-axis field was applied [see Fig. 7(f)], the highest sensitivity (25.5%) in magnetoresistance ratio variation occurred in the 800 nm wide nanowire. Additionally, the sensitivity in the switching field variation $\Delta H_c/H_{c_0}$ of the 150 nm nanowire can also be up to 27% when a *z*-axis field is applied [see Fig. 7(c)]. This sensitivity was much higher than the case when the field was applied in the *x* direction [see Fig. 7(a)]. A possible reason is given as follows.

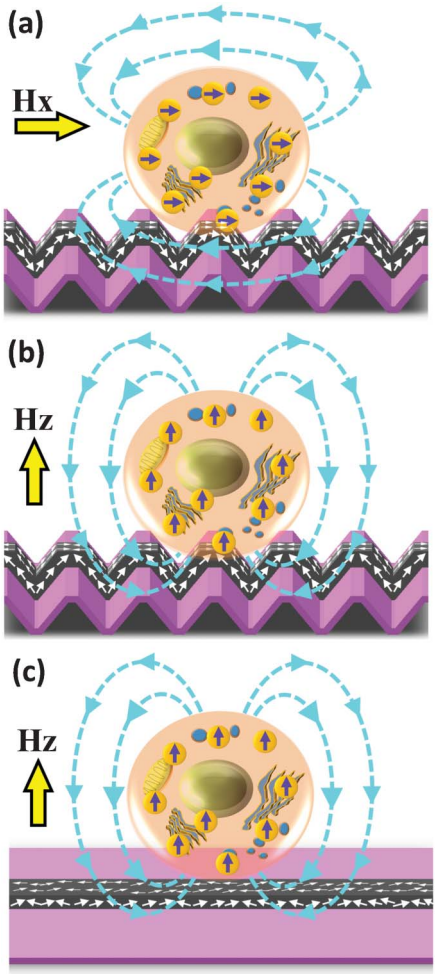

Fig. 8 Interactions between the stray field generated by the magnetic cell and the magnetic moments within the zigzag magnetic nanowires when the field was along (a) *x* axis and (b) *z* axis. (c) The interaction between the stray field and the magnetic moments of a flat-surfaced magnetic film.

Fig. 8 illustrates the measurement mechanism of the biosensor. When an external field is applied, a stray field is induced by the magnetized nanoparticles inside the cell. In Fig. 8(a), the non-uniform stray field is mostly opposed to the external field in the magnetic nanowire area, and therefore it requires a larger field for the nanowire to accomplish the switching. Comparing Fig. 8(a) and 8(b) where the field is applied along the *x* and *z* directions, respectively, it can be found that the magnetic flux density of the local stray field which can influence the nanowire is denser in Fig. 8(b) than in Fig. 8(a). This suggests that the stray field has more impact on the switching of the nanowire when the field is along the *z* axis, and therefore it is in this case that the biosensor has the highest sensitivity in detecting cells. In contrast, when a flat-surfaced device is used for detecting cells [see Fig. 8(c)], is hard to align the magnetic moment of the stray field generated by the magnetic cell along the *z* axis, which is the hard axis of the thin film, and it therefore suppresses the magnetoresistance signal change.

Table 1 Comparison between different types of magnetoresistance biosensors[b]

Sensor type	Sensor size	Magnetic label particle(s)	Label size (diameter)	Normalized signal magnitude[a]	Ability to attract analytes	Ref.
Our device	150–800 nm nanowire	Fe_3O_4	10 nm	1.74×10^{13}	Yes (single cell)	
AMR square ring	1×1 μm	Fe_3O_4	130 nm	6.73×10^{12}	Yes (magnetic particles)	29
Pseudo spin valve ring	4 μm (diameter)	Dynabeads M-450	4.5 μm	5.12×10^{12}	Not available	28
Spin valve ring	18 μm (diameter)	Dynabeads M-280	2.8 μm	3.17×10^{11}	Not available	41
Spin valve square film	2×16 μm	Nanomag-D	300 nm	4.35×10^{12}	Not available	42
GMR disk	200 μm (diameter)	Dynabeads M-280	2.8 μm	1.26×10^{11}	Not available	43

[a] Normalized signal magnitude ≡ $(\Delta MRratio/MRratio_0)/m$. [b] m: total magnetic moment of the magnetic label particle(s).

Table 1 summarizes the comparison between our designed magnetic zigzag nanowire biosensor and other different types of magnetoresistance biosensor. So far, most magnetoresistance biosensors are used for the detection of biomolecules rather than a single cell. From Table 1 it can be observed that the zigzag nanowire biosensor designed in this study not only can be used for single cell detection but also has the advantages of actively attracting and fixing the analyte (cell) thanks to the stray field generated by the corners of the magnetic zigzag nanowires. The designed biosensor also possesses much higher sensitivity, which can be determined by the normalized signal magnitude, compared to the other types of magnetoresistance biosensors listed in the table.

Conclusions

Existing magnetoresistance-based biosensors are generally flat surfaced, and cells might be flushed away quite easily by the fluidic flow on the chip or within the microfluidic channel, causing significant interference on the measured signals. The trench-structured substrate proposed in this study can fix the magnetic cells on the sensor surface, and meanwhile, the stray field generated by the corners of the magnetic nanowires has the function of actively attracting the magnetic cells. Additionally, this design also allows for multi-directional detection. It was observed that the highest switching field variation occurred in the 150 nm wide nanowire when the field was perpendicular to the substrate plane. On the other hand, the highest magnetoresistance ratio variation occurred in the 800 nm wide nanowire also when the field was perpendicular to the substrate plane. The zigzag biosensor proposed in this study has the advantages of higher flexibility, stability and sensitivity in detecting cells. This design can provide important information for future applications of cell detection using magnetic biosensors.

Acknowledgements

This work was supported partly by the ROC National Science Council Grant Numbers NSC 99-2112-M-007-016-MY3 and NSC 99-2112-M-007-015-MY3.

References

1 J. Llandro, J. J. Palfreyman, A. Ionescu and C. H. W. Barnes, *Med. Biol. Eng. Comput.*, 2010, **48**, 977–998.
2 J. Schotter, P. B. Kamp, A. Becker, A. Pühler, G. Reiss and H. Brückl, *Biosens. Bioelectron.*, 2004, **19**, 1149–1156.
3 L. Xu, H. Yu, M. S. Akhras, S. J. Han, S. Osterfeld, R. L. White, N. Pourmand and S. X. Wang, *Biosens. Bioelectron.*, 2008, **24**, 99–103.
4 D. L. Graham, H. A. Ferreira and P. P. Freitas, *Trends Biotechnol.*, 2004, **22**, 455–462.
5 S. J. Cho, D. Maysinger, M. Jain, B. Roder, S. Hackbarth and F. M. Winnik, *Langmuir*, 2007, **23**, 1974–1980.
6 R. Hintsche, C. Kruse, A. Uhlig, M. Paeschke, T. Lisec, U. Schnakenberg and B. Wagner, *Sens. Actuators, B*, 1995, **27**, 471–473.
7 S. Poyard, N. Jaffrezic-Renault, C. Martelet, S. Cosnier and P. Labbe, *Anal. Chim. Acta*, 1998, **364**, 165–172.
8 B. Ilic, D. Czaplewski, H. G. Craighead, P. Neuzil, C. Campagnolo and C. Batt, *Appl. Phys. Lett.*, 2000, **77**, 450.
9 D. L. Stokes, G. D. Griffin and T. Vo-Dinh, *Fresenius' J. Anal. Chem.*, 2001, **369**, 295–301.
10 S. Tombelli, M. Minunni and M. Mascini, *Methods*, 2005, **37**, 48–56.
11 S. J. Park, T. A. Taton and C. A. Mirkin, *Science*, 2002, **295**, 1503–1506.
12 S. Zhou, Q. Chen, X. Hu and T. Zhao, *J. Mater. Chem.*, 2012, **22**, 8263–8270.
13 C. P. Lee, H. Y. Tsai and M. F. Lai, *Appl. Phys. Lett.*, 2012, **100**, 264102.
14 M. F. Lai, C. Y. Chen, C. P. Lee, H. T. Huang, T. R. Ger and Z. H. Wei, *Appl. Phys. Lett.*, 2010, **96**, 183701.
15 I. M. Hsing, Y. Xu and W. Zhao, *Electroanalysis*, 2007, **19**, 755–768.
16 H. Gu, K. Xu, C. Xu and B. Xu, *Chem. Commun.*, 2006, 941–949.
17 J. Gao, H. Gu and B. Xu, *Acc. Chem. Res.*, 2009, **42**, 1097–1107.
18 J. Yang, C. H. Lee, J. Park, S. Seo, E. K. Lim, Y. J. Song, J. S. Suh, H. G. Yoon, Y. M. Huh and S. Haam, *J. Mater. Chem.*, 2007, **17**, 2695–2699.
19 J. Xie, G. Liu, H. S. Eden, H. Ai and X. Chen, *Acc. Chem. Res.*, 2011, **44**, 883–892.
20 N. Lee and T. Hyeon, *Chem. Soc. Rev.*, 2012, **41**, 2575–2589.
21 J. Dobson, *Drug Dev. Res.*, 2006, **67**, 55–60.
22 C. Sun, J. S. H. Lee and M. Q. Zhang, *Adv. Drug Delivery Rev.*, 2008, **60**, 1252–1256.

23 F. Dong, W. Guo, J. H. Bae, S. H. Kim and C. S. Ha, *Chem.–Eur. J.*, 2011, **17**, 12802–12808.
24 D. S. Choi, J. Park, S. Kim, D. H. Gracias, M. K. Cho, Y. K. Kim, A. Fung, S. E. Lee, Y. Chen, S. Khanal, S. Baral and J. H. Kim, *J. Nanosci. Nanotechnol.*, 2008, **8**, 2323–2327.
25 K. H. Bae, M. Park, M. J. Do, N. Lee, J. H. Ryu, G. W. Kim, C. Kim, T. G. Park and T. Hyeon, *ACS Nano*, 2012, **6**, 5266–2573.
26 D. R. Baselt, G. U. Lee, M. Natesan, S. W. Metzger, P. E. Sheehan and R. J. Colton, *Biosens. Bioelectron.*, 1998, **13**, 731–739.
27 M. M. Miller, G. A. Prinz, S. F. Cheng and S. Bounnak, *Appl. Phys. Lett.*, 2002, **81**, 2211.
28 J. Llandro, T. J. Hayward, D. Morecroft, J. A. C. Bland, F. J. Castaño, I. A. Colin and C. A. Ross, *Appl. Phys. Lett.*, 2007, **91**, 203904.
29 P. Vavassori, V. Metlushko, B. Ilic, M. Gobbi, M. Donolato, M. Cantoni and R. Bertacco, *Appl. Phys. Lett.*, 2008, **93**, 203502.
30 J. Schotter, P. B. Kamp, A. Becker, A. Pühler, D. Brinkmann, W. Schepper, H. Brückl and G. Reiss, *IEEE Trans. Magn.*, 2002, **38**, 3365–3367.
31 M. M. Miller, P. E. Sheehan, R. L. Edelstein, C. R. Tamanaha, L. Zhong, S. Bounnak, L. J. Whitman and R. J. Colton, *J. Magn. Magn. Mater.*, 2001, **225**, 138–144.
32 D. L. Graham, H. Ferreira, J. Bernardo, P. P. Freitas and J. M. S. Cabral, *J. Appl. Phys.*, 2002, **91**, 7786–7788.
33 S. K. Arya, K. C. Lee, D. B. Dah'alan, D. Rahman and A. R. A. Rahman, *Lab Chip*, 2012, **12**, 2362–2368.
34 D. G. Spiller, C. D. Wood, D. A. Rand and M. R. H. White, *Nature*, 2010, **465**, 736–745.
35 S. Zhao, X. Li and Y. M. Liu, *Anal. Chem.*, 2009, **81**, 3873–3878.
36 H. T. Huang, C. Y. Chen and M. F. Lai, *J. Appl. Phys.*, 2011, **109**, 07B315.
37 D. G. Grier, *Nature*, 2003, **424**, 810–816.
38 P. Y. Chiou, A. T. Ohta and M. C. Wu, *Nature*, 2005, **436**, 370–372.
39 G. F. Goya, T. S. Berquo, F. C. Fonseca and M. P. Morales, *J. Appl. Phys.*, 2003, **94**, 3520–3528.
40 P. Y. Wang, H. T. Yu and W. B. Tsai, *Biotechnol. Bioeng.*, 2010, **106**, 285–294.
41 J. D. Suh, S. D. Jung and M. A. Chung, *IEEE Trans. Magn.*, 2009, **45**, 2730–2732.
42 L. Lagae, R. Wirix-Speetjens, J. Das, D. Graham, H. Ferreira, P. P. F. Freitas, G. Borghs and J. De Boeck, *J. Appl. Phys.*, 2002, **91**, 7445–7447.
43 J. C. Rife, M. M. Miller, P. E. Sheehan, C. R. Tamanaha, M. Tondra and L. J. Whitman, *Sens. Actuators, A*, 2003, **107**, 209–218.

